Atmos. Meas. Tech. Discuss., 8, 2143–2189, 2015
www.atmos-meas-tech-discuss.net/8/2143/2015/
doi:10.5194/amtd-8-2143-2015

Atmospheric Measurement Techniques Discussions
Open Access

Optical depths of semi-transparent cirrus clouds over oceans from CALIPSO infrared radiometer and lidar measurements, and an evaluation of the lidar multiple scattering factor

A. Garnier[1], J. Pelon[2], M. A. Vaughan[3], D. M. Winker[3], C. R. Trepte[3], and P. Dubuisson[4]

[1]Science Systems and Applications Inc., Hampton, VA, USA
[2]Laboratoire Atmosphères, Milieux, Observations Spatiales, UPMC-UVSQ-CNRS, Paris, France
[3]NASA Langley Research Center, Hampton, VA, USA
[4]Laboratoire d'Optique Atmosphérique, Université Lille 1, Lille, France

Received: 31 December 2014 – Accepted: 16 February 2015 – Published: 25 February 2015

Correspondence to: A. Garnier (anne.garnier@latmos.ipsl.fr)

Published by Copernicus Publications on behalf of the European Geosciences Union.

Abstract

This paper provides a detailed evaluation of cloud absorption optical depths retrieved at 12.05 µm and comparisons to extinction optical depths retrieved at 0.532 µm from perfectly co-located observations of single-layered semi-transparent cirrus over ocean made by the Imaging Infrared Radiometer (IIR) and the Cloud and Aerosol Lidar with Orthogonal Polarization (CALIOP) flying on-board the CALIPSO (Cloud-Aerosol Lidar and Infrared Pathfinder Satellite Observations) satellite. The blackbody radiance taken in the IIR Version 3 algorithm is evaluated, and IIR retrievals are corrected accordingly. IIR infrared absorption optical depths are then compared to CALIOP visible extinction optical depths when the latter can be directly derived from the measured apparent 2-way transmittance through the cloud. Numerical simulations and IIR retrievals of ice crystal sizes suggest that the ratios of CALIOP extinction and IIR absorption optical depths should remain roughly constant with respect to temperature. Instead, these ratios are found to increase quasi-linearly by about 40 % as the temperature at the layer centroid altitude decreases from 240 to 200 K. This behavior is explained by variations of the multiple scattering factor η_T to be applied to correct the measured transmittance, which is taken equal to 0.6 in the CALIOP Version 3 algorithm, and which is found here to vary with temperature (and hence cloud particle size) from $\eta_T = 0.8$ at 200 K to $\eta_T = 0.5$ at 240 K for clouds with optical depth larger than 0.3. The revised parameterization of η_T introduces a concomitant temperature dependence in the simultaneously derived CALIOP lidar ratios that is consistent with observed changes in CALIOP depolarization ratios and particle habits derived from IIR measurements.

1 Introduction

Cirrus clouds are widely distributed over the globe. Most cirrus exhibit compensating thermal and solar radiative effects, with the net effect depending on optical depth and particle size (Berry and Mace, 2014). Thus, well-validated global measurements

AMTD
8, 2143–2189, 2015

of cirrus optical depths and properties are required to reliably assess their radiative impacts (Sassen et al., 2008). Ideally, these measurements would be validated using wholly independent retrievals from different instruments using different measurement techniques that have largely or wholly independent sources of uncertainty. While this multi-instrument approach is conceptually straightforward, there are typically a number of practical difficulties (e.g., accurate spatial and temporal matching) that make full realization of the technique somewhat challenging. The sensor design and selection for the Cloud-Aerosol Lidar and Infrared Pathfinder Satellite Observations (CALIPSO) mission (Winker et al., 2010) obviates most of these concerns. The instrumentation aboard the CALIPSO satellite includes CALIOP (i.e., the Cloud and Aerosol Lidar with Orthogonal Polarization), a two-wavelength (532 and 1064 nm), polarization-sensitive (at 532 nm) elastic backscatter lidar (Hunt et al., 2009), a 3-channel Imaging Infrared Radiometer (IIR) operating in the 8–12 µm thermal infrared spectral range (Corlay et al., 2000), and a Wide Field Camera (WFC) operating in the visible domain (Pitts et al., 2007). These instruments are assembled in a staring and near-nadir-looking configuration. The cross-track swaths of the passive sensors are centered on the lidar footprint so that observations from all three instruments are almost perfectly collocated in both time and space. The combined measurements thus allow highly detailed comparison studies that are not subject to collocation uncertainties or concerns about view angle differences.

CALIOP cirrus visible optical depths are total extinction optical depths retrieved using one of two different and totally independent techniques. The first method is the so-called "constrained retrieval", in which the "apparent" cloud optical depth is derived from the 2-way transmittance as measured from molecular scattering above and below the cloud layer. The cloud optical depth is then derived with an instrument-specific correction for multiple scattering effects. Direct measurements of apparent optical depth can also be obtained in the presence of some well-characterized secondary scattering layer lying beneath the cirrus. Among the secondary scattering targets that have been recently identified for use in constrained retrievals are ocean surfaces (Josset et al.,

AMTD
8, 2143–2189, 2015

2012) and opaque water clouds (Hu et al., 2007). In the second method, called "unconstrained retrievals" (Young and Vaughan, 2009), optical depth estimates are derived using a priori assumptions about the layer extinction-to-backscatter ratio, a quantity also known as the lidar ratio, S_{cal}, and about the layer multiple scattering factor, η. The accuracy of the optical depth estimates obtained in this manner depends critically on the accuracy of the assumed apparent lidar ratio S^*, which is defined as the product of S_{cal} and η.

The only constrained retrieval target currently implemented in the standard CALIOP analyses is clear air. It has long been recognized that when the scattering characteristics of the ambient molecular atmosphere are well known (e.g., from models or rawinsonde measurements), the apparent two-way transmittance of a layer can be measured directly whenever sufficiently clean air is found immediately above and below the layer (Young, 1995; Elouragini and Flamant, 1996; del Guasta, 1998; Chen et al., 2002; Yorks et al., 2011). The main advantage of the "constrained retrieval" technique is that it does not require an a priori assumption about the apparent lidar ratio. On the contrary, because the layer apparent optical depth has been measured, accurate estimates of S^* can be retrieved by applying the constrained retrieval technique to suitable CALIOP data (Young and Vaughan, 2009; Young et al., 2013).

In order to extend the constrained approach, Platt (1973) proposed a combined radiometric and lidar retrieval to more fully characterize cirrus cloud properties. In this paper, the relationship between infrared absorption and visible extinction optical depth is investigated in detail, based on heritage from the pioneering work of C. M. R. Platt in the 1970s, which is applied here to global space-borne observations. Infrared absorption optical depths retrieved from IIR observations of single-layered cirrus clouds at 12.05 µm are compared to the visible optical depths derived by applying CALIOP's constrained retrieval technique to precisely collocated measurements of the same cloud. Based on a detailed analysis of these comparisons, a new relationship describing the temperature-dependent effect of multiple scattering in the CALIOP retrievals is derived and discussed. The technique used to retrieve cirrus emissivity and absorption op-

AMTD
8, 2143–2189, 2015

tical depths from the CALIPSO IIR measurements is described in depth by Garnier et al. (2012a). A substantial review of this method is given below. These analyses use version 3 CALIOP Level 2 5 km cloud layer products and the corresponding version 3 IIR Level 2 track products (Powell et al., 2013). The paper is constructed as follows. Retrieval techniques, sources of uncertainty, and expected ratios between retrievals in the visible and in the infrared are presented in Sect. 2. In the IIR algorithm, emissivity and absorption optical depth are retrieved assuming an isothermal cloud layer of equivalent temperature inferred from the CALIOP layer detection algorithm. This technique is assessed in Sect. 3. CALIOP and IIR retrievals are then compared and discussed in Sect. 4. Using analyses organized around the specifics of each algorithm and cloud characteristics such as optical depth and temperature, the CALIOP multiple scattering factor derived from these comparisons is evaluated. Section 5 provides a summary of the work and presents our conclusions about the effectiveness of these multi-sensor analyses.

2 CALIPSO retrieval techniques

2.1 CALIOP

A detailed overview of CALIOP retrievals can be found in Winker et al. (2009) and the works cited therein. Here we provide only a brief synopsis. The CALIOP Level 1 calibrated 532 nm total attenuated backscatter profiles are used to detect scattering layers with horizontal resolutions of 5, 20 or 80 km, defined by the amount of averaging required to detect the layers (Vaughan et al., 2009). After discriminating between clouds and aerosols (Liu et al., 2009), cloud layers are further classified according to thermodynamic phase and crystal habit as water clouds, randomly-oriented ice clouds, or horizontally-oriented ice clouds (Hu et al., 2009). Cirrus cloud optical depths are then retrieved by CALIOP's Hybrid Extinction Retrieval Algorithms (HERA) using a layer-constant multiple scattering factor of $\eta = 0.6$ (Young and Vaughan, 2009).

AMTD
8, 2143–2189, 2015

In version 3 of the CALIPSO data products, the HERA module identifies those layers for which constrained solutions are considered feasible by requiring that the estimated relative uncertainty in the derived lidar ratio be less than 40 %. The apparent two-way transmittance of these layers can then be obtained directly from the ratio of the mean attenuated scattering ratios in clear air regions above and below the cloud; i.e., $T^2_{\text{apparent}} = \langle R' \rangle_{\text{below}} / \langle R' \rangle_{\text{above}}$. The visible optical depth is simply

$$\tau_{\text{vis}} = \frac{-\ln\left(T^2_{\text{apparent}}\right)}{2\eta} \quad (1)$$

where division by η represents the required correction of the measured transmittance for multiple scattering. Because solar background illumination injects large amounts of noise into the CALIOP daytime backscatter signal, the signal-to-noise ratios (SNR) needed to satisfy this rather stringent requirement are almost never found in CALIOP daytime measurements. As a consequence, CALIOP version 3 constrained retrievals are available almost exclusively during nighttime (Young and Vaughan, 2009). Uncertainties in CALIOP optical depth retrievals are described extensively in Young et al. (2013).

2.2 IIR

The IIR is a passive instrument providing calibrated radiances in 3 channels in the atmospheric window (8.65, 10.6, and 12.05 µm), with a medium spectral resolution of about 1 µm, and a spatial resolution of 1 km per pixel over a 69 km swath. IIR radiances are sensitive to absorbing clouds and to mineral dusts. The IIR 12.05 µm channel, which exhibits the largest absorption by cirrus clouds, is chosen for this analysis. The pixels located at the center of the 69 km swath are precisely collocated with CALIOP lidar foot-print, and thus a vertically resolved description of the atmospheric column associated with passive IIR observations is obtained from CALIOP active measurements. IIR retrievals rely on cloud and aerosol detections from CALIOP, and as IIR

AMTD
8, 2143–2189, 2015

observations are not vertically resolved, the most suitable scenes are those containing only one single cloud layer in the column. Scenes containing low opaque water clouds, also analyzed by the IIR algorithm, are not included in this study. In addition, scenes containing depolarizing aerosol layers such as mineral dust are discarded.

Cloud absorption is characterized through its emissivity ε, where (Platt and Gambling, 1971; Platt, 1973; Garnier et al., 2012a)

$$\varepsilon = \frac{R_{\mathrm{BG}} - R_{\mathrm{m}}}{R_{\mathrm{BG}} - R_{\mathrm{BB}}}, \tag{2}$$

and cloud absorption optical depth τ_{a} is subsequently derived using

$$\tau_{\mathrm{a}} = -\ln(1-\varepsilon). \tag{3}$$

In Eq. (2), R_{m} is the measured calibrated radiance, R_{BG} is the background radiance at the top of the atmosphere that would be observed in the absence of the studied cloud, and R_{BB} is the radiance of a blackbody source located at the cloud radiative altitude.

Uncertainty in the emissivity includes 3 components associated with errors on R_{m}, R_{BG}, and R_{BB} and is inversely proportional to the radiative contrast R_{BG}–R_{BB} (Garnier et al., 2012a). In other words, the colder the cloud with respect to the underlying scene, the smaller the uncertainty in the emissivity retrievals. Similarly, the error $\mathrm{d}\tau_{\mathrm{a}}$ on τ_{a} is written

$$\mathrm{d}\tau_{\mathrm{a}} = (1/1-\varepsilon)\cdot \mathrm{d}R'_{\mathrm{m}} + (\varepsilon/1-\varepsilon)\cdot \mathrm{d}R'_{\mathrm{BB}} + \mathrm{d}R'_{\mathrm{BG}}, \tag{4}$$

where the quantity $\mathrm{d}R'_x$ is the error on the radiance R_x weighted by the inverse of the radiative contrast, and where the subscript x refers to m, BB or BG.

In Eq. (4), each term $\mathrm{d}R'_x$ is related to the error on the equivalent brightness temperature $\mathrm{d}T_x$ as

$$\mathrm{d}R'_x = \frac{\partial R_x}{\partial T}\cdot \mathrm{d}T_x \cdot \frac{1}{R_{\mathrm{BG}} - R_{\mathrm{BB}}}. \tag{5}$$

AMTD
8, 2143–2189, 2015

Each term in Eq. (4) represents the sensitivity of τ_a to each of the 3 quantities involved in the computation of τ_a. Uncertainty estimates are derived after assessing the random and systematic errors dT_m, dT_{BG}, and dT_{BB}. As an illustration, Fig. 1 shows the relative sensitivity $d\tau_a/\tau_a$ to $dT_m = -0.3\,K$, $dT_{BG} = +0.5\,K$, and $dT_{BB} = +2\,K$ for cirrus clouds. The rationale for this choice of values is given below. The variation $d\tau_{a,\,BG}$ due to a variation dR'_{BG} of the weighted background radiance does not depend on ε, and the relative variation $d\tau_{a,\,BG}/\tau_a$ (dashed line) decreases with τ_a, more rapidly for $2\tau_a$ smaller than 0.3. A similar behavior is seen for the measured radiance (dotted line). However, the relative variation of τ_a due to a variation of dT_{BB} increases steadily with τ_a (solid line).

The on-board measured calibrated radiances have been validated by comparison with airborne observations (Sourdeval et al., 2012). The value $dT_m = \pm 0.3\,K$ is based on the noise equivalent differential temperature and calibration accuracy as assessed by the Centre National d'Etudes Spatiales (CNES) and is taken as a random error in the final uncertainty assessment.

Both R_{BG} and R_{BB} in Eq. (2) are inferred in synergy with CALIOP observations and so too are the respective uncertainty estimates dT_{BG} and dT_{BB} (Garnier et al., 2012a).

The background radiance, R_{BG}, is preferably retrieved from cloud-free observations in neighboring pixels along track as identified by CALIOP at a distance chosen to be smaller than 100 km from the analyzed pixel. If these conditions are not found, R_{BG} is computed using the FASt RADiative (FASRAD) transfer model (Dubuisson et al., 2005) and ancillary atmospheric and surface data from the GEOS 5 model of the Global Modeling and Assimilation Office (Rienecker et al., 2008). These two ensembles of retrievals will be evaluated separately as their sources of uncertainty are different. For the first ensemble, that is R_{BG} measured in neighboring pixels, R_{BG} is derived purely from observations and is expected to be unbiased with respect to measured radiances. A random error dT_{BG} is assumed, which is arbitrarily augmented from 0.3 to 0.5 K to account for possible differences between the studied area and the nearby non-cloudy area.

AMTD
8, 2143–2189, 2015

The blackbody radiance R_{BB} is computed from the FASRAD model and the thermodynamic temperature, T_c, at the centroid altitude, Z_c, of the CALIOP attenuated backscatter profile at 532 nm within the cloud layer (Vaughan et al., 2005). This parameter, derived from Level 1 CALIOP observations, is reported in the CALIOP 5 km layer product and is available as an input to the IIR Level 2 operational algorithm. In order to assess possible systematic errors dT_{BB}, the cloud radiative temperature, T_r, can be computed a posteriori from CALIOP extinction profiles and compared with the temperature T_c. This analysis is detailed in Sect. 3. Subsequent systematic errors on IIR optical depth and corrections will also be discussed. An additional random error of $dT_{BB} = 2$ K is assumed to account for possible errors in the atmospheric model.

Even though the IIR analyses take advantage of spatial information (e.g. cloud heights) derived from CALIOP collocated vertical profile observations, the IIR cloud optical properties retrievals are entirely independent from the CALIOP optical properties retrievals. The measurement techniques used by the two sensors rely on different physical principles and hence are subject to very different sources of uncertainty. The expected relationship between CALIOP and IIR optical depths is presented in the following section.

2.3 Simulated relationships between CALIOP and IIR optical depths

Ratios of CALIOP cirrus visible extinction optical depth τ_{vis} to IIR absorption optical depth τ_a at 12.05 µm are simulated using the FASDOM radiative transfer model (Dubuisson et al., 2005, 2008) for an isothermal cloud and ice crystal optical properties retrieved from pre-computed tables (Yang et al., 2005). Figure 2 shows simulated τ_{vis}/τ_a ratios for clouds composed of hexagonal solid columns and of aggregates by taking $\tau_a = 0.25$. Effective diameters (D_e) (x axis) are defined as 3/2 times the ratio of volume to projected area (Mitchell et al., 2002). As seen in Fig. 2, τ_{vis}/τ_a increases as D_e increases for D_e larger than 10–15 µm, from 1.7–1.9 at D_e equal to 20 µm up to 2.07 at D_e equal to 140 µm. These simplified simulations, which assume mono-disperse particle size distributions, are sufficient to assess the sensitivity of τ_{vis}/τ_a to ice crystal

AMTD
8, 2143–2189, 2015

size and habit and to establish that τ_{vis}/τ_a is expected to be around 2. A more detailed discussion is given in Sect. 4. It is to be noted that τ_a is not, strictly speaking, an absorption optical depth as it includes a small contribution from multiple scattering, which becomes more important as optical depth grows larger. Simulations show that τ_a is increased by less than 3 % with respect to pure absorption optical depth at τ_a equal to 1.25, or τ_{vis} around 2.5, which is the maximum value attained by the semi-transparent cirrus clouds considered in this study.

3 Cloud radiative temperature

As seen in Sect. 2, cloud effective emissivity and hence infrared absorption optical depth are retrieved through a simple relationship (see Eq. 2) by considering an isothermal cloud of blackbody radiance R_{BB} computed using the centroid temperature T_c at the centroid altitude Z_c. In this section, systematic errors in the blackbody brightness temperature dT_{BB} resulting from this assumption are quantified. To do so, the cloud radiative temperature T_r is computed a posteriori from CALIOP extinction profiles and compared to T_c, so that ultimately IIR retrievals can be corrected using Eqs. (4) and (5).

CALIOP extinction profiles are reported at 5 km horizontal resolution and are derived from the exact same attenuated backscatter profiles that are used to compute the centroid altitudes reported in the 5 km layer products. As the intent is to evaluate IIR retrievals, analyses are conducted for single-layered semi-transparent cirrus clouds over ocean. Data selection is further restricted to the subset of cirrus clouds composed of randomly oriented ice (ROI) crystals for which the ice-water phase classification is reported with high confidence. In addition, possible contamination from mixed-phase clouds is minimized by restricting the analysis to clouds whose temperature at base altitude is colder than −20 °C (Hu et al., 2010). CALIOP optical depths and extinction profiles are retrieved from the constrained technique described previously. The time period covers 12 months in 2008.

AMTD
8, 2143–2189, 2015

Each cloud is composed of a number n of vertical bins i of resolution δz, with $i = 1$ to $i = n$ extending from base to top. Emissivity in bin i is noted $\varepsilon(i)$ and absorption optical depth derived from Eq. (3) is $\tau_a(i)$. By applying Eq. (2) successively to each of the bins, from cloud base to cloud top, it is found that the cloud blackbody radiance R_{BB} can be expressed as

$$R_{BB} = \frac{\sum_{i=1}^{i=n} \varepsilon(i) \cdot R_{BB}(i) \cdot e^{-\sum_{j=i+1}^{j=n+1} \tau_a(j)}}{\sum_{i=1}^{i=n} \varepsilon(i) \cdot e^{-\sum_{j=i+1}^{j=n+1} \tau_a(j)}}, \quad (6)$$

where $R_{BB}(i)$ is the blackbody radiance of bin i of thermodynamic temperature $T(i)$, and where τ_a $(n+1)$ represents absorption above the cloud.

The denominator in Eq. (6) represents the cloud emissivity. The cloud blackbody radiance can be seen as the centroid radiance of the attenuated emissivity profile, with the attenuation term corresponding to the infrared transmittance above the bin i. This expression has been validated by comparing R_{BB} from Eq. (6) and from the FASRAD model. In Eq. (6), absorption by gases such as water vapor and ozone in the cirrus cloud is neglected, so that absorption is assumed to be purely due to the cloud. This simplification has no impact on the result for τ_a larger than 0.2 and otherwise biases R_{BB} by only 0.4 K of equivalent brightness temperature when τ_a tends to zero. Assuming a ratio r between CALIOP visible optical depth τ_{vis} and IIR absorption optical depth τ_a, Eq. (6) can be re-written as a function of the CALIOP cloud extinction coefficient α (in km^{-1}) and r, as

$$R_{BB} = \frac{\sum_{i=1}^{i=n} (1 - e^{-[\alpha(i) \cdot \delta z / r]}) \cdot R_{BB}(i) \cdot e^{-\sum_{j=i+1}^{j=n+1} [\alpha(j) \cdot \delta z / r]}}{\sum_{i=1}^{i=n} (1 - e^{-[\alpha(i) \cdot \delta z / r]}) \cdot e^{-\sum_{j=i+1}^{j=n+1} [\alpha(j) \cdot \delta z / r]}}. \quad (7)$$

The temperature T_r is derived from the blackbody radiance R_{BB} computed using Eq. (7). The ratio r is taken equal to 2 based on the simulations shown in Sect. 2.3, as well as

AMTD
8, 2143–2189, 2015

$2 \pm 20\,\%$ to evaluate the sensitivity of R_{BB} to r. The vertical resolution δz is equal to 0.06 km in the CALIOP profiles products.

On the other hand, the centroid altitude Z_c can be written as

$$Z_c = \frac{\sum_{i=1}^{i=n} Z(i) \cdot (\beta_{part}(i) + \beta_{mol}(i)) \cdot e^{-2\sum_{j=i}^{j=n}[\eta\alpha_{part}(j)+\alpha_{mol}(j)]\cdot\delta z}}{\sum_{i=1}^{i=n} (\beta_{part}(i) + \beta_{mol}(i)) \cdot e^{-2\sum_{j=i}^{j=n}[\eta\alpha_{part}(j)+\alpha_{mol}(j)]\cdot\delta z}} \quad (8)$$

where $Z(i)$ is the altitude of bin i, $\beta_{part}(i)$ and $\beta_{mol}(i)$ are, respectively, the particulate and molecular components of the total backscatter (in $sr^{-1}\,km^{-1}$), $\alpha_{part}(i)$ and $\alpha_{mol}(i)$ are, respectively, the particulate and molecular extinction coefficients (in km^{-1}), and η represents the required correction for multiple scattering introduced in Sect. 2.1. Equation (8) exhibits interesting similarities with Eq. (7). As radiance and altitude vary quasi-linearly with temperature within a few kilometer deep layer, Eqs. (7) and (8) are effectively two different weighted averages of the cloud temperature profile. In both cases, the weight is composed of the product of a transmittance term and of a multiplying term. For cirrus clouds of sufficient optical depth, the molecular contribution is weak compared to the particulate one, and the transmittance term in Eq. (8) is driven by $2\eta\alpha(j)$ or $1.2\alpha(j)$ assuming $\eta = 0.6$ for CALIOP observations, which is larger than $\alpha(j)/r$ in Eq. (7), or $\alpha(j)/2$ if $r = 2$. Thus, the smaller transmittance term in Eq. (8) compared to the one in Eq. (7) tends to provide Z_c higher than the radiative cloud altitude for observations from the top of the atmosphere. However, this is partly compensated by the multiplying terms. Indeed, in Eq. (8), the multiplying term is roughly proportional to the bin absorption optical depth $\tau_a(i) = \alpha(i) \cdot \delta z/r$, because the lidar ratio is taken constant in CALIOP extinction retrievals (Young and Vaughan, 2009). Therefore, the multiplying term in Eq. (8) can be seen as $\tau_a(i)$, which is larger than the multiplying term in Eq. (7), that is the emissivity $\varepsilon(i)$.

Overall, the temperature T_r derived from Eq. (7) is found to be warmer than the temperature T_c derived from Eq. (8) as seen in Fig. 3a, where mean $T_r - T_c$ differences are plotted against $2\tau_a$ for several ranges in cloud geometric thicknesses Δz from 1–2 km

AMTD
8, 2143–2189, 2015

up to 7–8 km (colored lines), and for all observations (black line). The $T_r - T_c$ differences represent systematic errors dT_{BB} on the blackbody brightness temperature used in the IIR standard retrievals. They are primarily driven by the cloud geometric thickness Δz and increase quasi-linearly with optical depth ($2\tau_a$) for a given Δz, with a slope close to zero for Δz in 1–2 km and that increases up to 1.5 K per unit optical depth for Δz between in 7–8 km. On average, the bias increases with $2\tau_a$ (black curve) from 0.5 to 3 K because optical depth and geometric thickness are not fully independent. Standard deviations are between 0.2 and 1.5 K (Fig. 3b) and include variability due to the fact that $T_r - T_c$ varies with the shape of the extinction profile for a given optical depth and a given geometric thickness. Biases shown in Fig. 3a have been retrieved assuming an a priori value $r = 2$. Sensitivity to this assumption is seen in Fig. 4, showing relative variations $\Delta T_r/(T_r - T_c)$ of $T_r - T_c$ when r is changed to 2.4 ($\Delta r = +20\,\%$, solid lines) and to 1.6 ($\Delta r = -20\,\%$, dashed lines), to cover a range of possible values according to the simulations (Fig. 2). As will be shown in Sect. 4, assuming r between 1.6 and 2.4 also allows covering the range of retrieved values. Increasing the ratio $r = \tau_{vis}/\tau_a$ does decrease τ_a as τ_{vis} is set from CALIOP retrievals, and the radiative temperature is increased ($\Delta T_r/(T_r - T_c)$ is positive). The opposite behavior is found when the ratio r is decreased. The estimated bias $dT_{BB} = T_r - T_c$ shown in Fig. 3a for $r = 2$ is found to vary by less than 16 % in the worst case, which is for $2\tau_a = 2.5$ and $\Delta r = -20\,\%$. Therefore, the bias dT_{BB} is estimated in the following by taking $r = 2$.

Correcting for a bias dT_{BB} ranging between 0.5 K at $2\tau_a \approx 0$ and 7 K at $2\tau_a = 2$ as seen in Fig. 3a induces a relative increase of τ_a between 0.5 and 17 % according to Fig. 1 and, on average, the largest increase is 7 % for $dT_{BB} = 3$ K at $2\tau_a = 2$. In the following, CALIOP and IIR retrievals will be compared before and after correcting IIR absorption optical depths for those biases, in order to assess the impact on the comparisons.

AMTD
8, 2143–2189, 2015

4 Comparison of IIR and CALIOP retrievals

CALIOP and IIR cirrus retrievals are evaluated through ratios of CALIOP visible optical depth τ_{vis} to IIR absorption optical depth τ_a. Data selection is the same as in Sect. 3. IIR absorption optical depths, reported at 1 km pixel resolution under the lidar track in the Level 2 products, are averaged to a 5 km horizontal resolution to match the resolution at which CALIOP optical depth is reported in the 5 km cloud layer products. Median τ_{vis}/τ_a ratios during 2008 in the 25° S–25° N latitude band are plotted against $2\tau_a$ in Fig. 5. Figure 5a is from the standard products whereas Fig. 5b is obtained with τ_a corrected by using the cloud blackbody radiance R_{BB} derived from CALIOP extinction profiles as described in Sect. 3. In order to simultaneously evaluate biases due to the background radiance R_{BG} as presented in Sect. 2, results are plotted by segregating type 1 clouds, defined as the clouds for which a measured R_{BG} is available and used to retrieve τ_a (solid lines), from type 2 clouds, for which R_{BG} is from computations (dashed lines). Furthermore, retrievals from computed R_{BG} are also plotted for type 1 clouds (dotted lines), for comparison with the standard retrievals (solid line). Finally, the τ_{vis}/τ_a ratios are shown for several ranges in centroid temperature T_c. Figure 5c shows the number of samples used to build the statistics. The standard deviation of the τ_{vis}/τ_a ratios plotted in Fig. 5d is found similar when τ_a is from standard products or corrected for the cloud radiative temperature. Figure 5 shows that the median τ_{vis}/τ_a ratios are overall within the ranges of expected values according to the simulations shown in Fig. 2. Figure 5 also contains pieces of information about systematic errors on IIR and CALIOP retrievals, which are discussed first. The retrieved τ_{vis}/τ_a ratios and their variations with T_c as seen in both Fig. 5a and b are discussed afterwards.

4.1 Systematic errors: IIR

τ_{vis}/τ_a ratios derived for type 1 clouds from measured R_{BG} (Fig. 5, solid lines) are expected to be the most accurate because they are the most constrained by IIR observations. For these exact same clouds, τ_a from computed R_{BG} (dotted lines) differs from

AMTD
8, 2143–2189, 2015

τ_a from measured R_{BG} (solid line) by less than 2 % at $2\tau_a = 0.7$. As, according to Fig. 1, an error $dT_{BG} = 0.5$ K induces a relative error in τ_a equal to 3.5 % at $2\tau_a = 0.7$, this indicates a bias $dT_{BG} = 0.3$ K in the computations. On the other hand, as seen in Sect. 3, the correction of R_{BB} increases τ_a and as expected, the τ_{vis}/τ_a ratios in Fig. 5b are smaller than in Fig. 5a. For type 1 clouds, it is seen that the corrected R_{BB} decreases the τ_{vis}/τ_a ratio by less than 5 % for the largest optical depths.

Type 1 and type 2 clouds are mutually exclusive and appear to have different properties. The fraction of type 2 clouds is larger at colder temperatures (see Fig. 5c, dashed lines), and the number of type 1 clouds is not significant at 193–203 K. In addition, most of the type 1 clouds have a geometric thickness Δz between 1.5 and 3 km whereas type 2 clouds are deeper, with Δz mostly between 3 and 6 km and up to 8 km (not shown). Therefore, the blackbody correction is overall larger for type 2 clouds than for type 1 ones (Fig. 3a). As a result, a better agreement between τ_{vis}/τ_a from type 1 (dotted lines) and from type 2 (dashed) clouds is clearly noted after correction (Fig. 5b) than before correction (Fig. 5a) for the largest $2\tau_a$ between 1 and 1.5. After correction, the overall difference is 1 to 5 % at $2\tau_a = 0.7$, which is possibly due to additional biases of 0.2 to 0.8 K (Fig. 1) in the computed R_{BG}, even though actual differences of the τ_{vis}/τ_a ratios cannot be ruled out as two distinct ensembles of clouds are compared. Further analyses of the differences between observations and computations are being conducted to help inform and improve future versions of the IIR science data products.

The τ_{vis}/τ_a ratio exhibits a sharp decrease of about 40 % from $2\tau_a = 0.3$ to $2\tau_a = 0.5$ for each temperature range, and decreases slowly by about 10 % from $2\tau_a = 0.7$ to $2\tau_a = 2.5$. This behavior is observed for both type 1 and type 2 clouds. As for type 1 clouds (solid lines) R_{BG} is from neighboring observations, biases in IIR τ_a retrievals do not seem to be a tenable explanation. As a consequence, possible biases in CALIOP retrievals are investigated in the following section.

AMTD
8, 2143–2189, 2015

4.2 Systematic errors: CALIOP

In the version 3 data products, CALIOP optical depth is retrieved using the constrained technique only when the estimated relative uncertainty in the derived lidar ratio is less than 40 %. This relative uncertainty increases rapidly for small optical depths (Young et al., 2013) and typically, optical depths smaller than 0.3 are retrieved using the unconstrained technique. Because the signal is noisy, optical depth distributions derived from constrained retrievals are increasingly truncated as actual optical depth decreases, because a larger fraction of these small optical depths do not satisfy the estimated relative uncertainty requirement and thus are excluded from the sample data set. This leads to an increasing high bias in constrained optical depths τ_{vis} as optical decreases, which explains the sharp increase of the τ_{vis}/τ_a ratio as $2\tau_a$ decreases.

When the constrained technique is not selected, optical depth is retrieved using the unconstrained technique and a default lidar ratio. Nevertheless, whenever measurements of layer two-way transmittance can be made, this apparent transmittance is also reported in the CALIOP products. Optical depths for these layers can then be directly inferred, as is done for the standard constrained retrievals. An extended set of CALIOP optical depth measurements is thus obtained, still limited to nighttime data, which is compared to IIR τ_a retrievals. Median τ_{vis}/τ_a ratios for the standard constrained retrievals (thin lines) and for the extended optical depth data set (thick lines) are shown in Fig. 6a for type 1 clouds only for more clarity, after correction of IIR τ_a for the cloud radiative temperature, and again, for several ranges in temperature T_c. Associated standard deviations are plotted in Fig. 6b. For the extended data set (thick lines), the τ_{vis}/τ_a ratios now increase steadily from the largest optical depths down to $2\tau_a = 0.3$, suggesting that the extended CALIOP optical depth distributions are not as biased for this data set. A sharp increase of the τ_{vis}/τ_a ratio is still seen for $2\tau_a$ smaller than 0.3, as this ratio of two small numbers becomes more sensitive to small residual biases. In addition, distributions are again truncated, because non-physical negative optical depths due to random noise are discarded from the analysis. Standard deviations of the τ_{vis}/τ_a ra-

AMTD
8, 2143–2189, 2015

tios are larger for the extended than for the standard constrained data set, suggesting larger random errors because CALIOP distributions are not as severely truncated in the former case. Implications are threefold. First, this confirms that IIR τ_a retrievals are not biased by unidentified issues. Secondly, this highlights a systematic bias at any temperature in CALIOP standard constrained retrievals (thin lines) for optical depths smaller than about 0.6, which is of the order of +50 % at $2\tau_a = 0.3$. This translates into similar relative biases in the retrieved lidar ratios, which is of importance when cirrus lidar ratios derived from constrained retrievals are used to evaluate the default lidar ratio used in unconstrained retrievals (Garnier et al., 2012b). Finally, this shows that the constrained technique could be improved, in the mean, by relaxing the threshold in the relative lidar ratio uncertainties used in version 3 of the CALIOP algorithm, notwithstanding the large dispersion.

4.3 Retrieved τ_{vis}/τ_a ratios

In the following, the retrieved median τ_{vis}/τ_a ratios are discussed. Results obtained after τ_a is corrected for cloud radiative temperature are considered. As seen in Figs. 5 and 6, the ratios are found to increase by about 10 % as the temperature T_c decreases by 10 K. The ratios derived from type 1 clouds are found between 1.6 at 233–243 K and 2.1 at 203–213 K, with a standard deviation of the order of 0.3 at $2\tau_a$ larger than 1. For type 2 clouds, the ratios are larger by 2 to 5 %, which could be partly explained by possible biases on IIR τ_a retrievals. Nevertheless, as both type 1 and type 2 clouds exhibit the same behavior with respect to temperature, they will be combined in the following analyses. To reduce the impact of biases, subsequent analyses are limited to cases for which $2\tau_a$ is larger than 0.3. Also, CALIOP extended optical depth retrievals are chosen to avoid biases in CALIOP standard constrained retrievals. For a given temperature, the ratios decrease by about 10 % from $2\tau_a = 0.3$ to $2\tau_a = 2$, as seen in Fig. 6a. This may be due partly to an increasing contribution of multiple scattering in τ_a, yet expected to not increase by more than 2 % according to simulations performed on numerous crystal habits.

AMTD
8, 2143–2189, 2015

The clear dependence of τ_{vis}/τ_a on temperature T_c is interesting. According to the simulations shown in Fig. 2 for the 12.05 µm IIR channel, for effective diameters larger than 10–15 µm, the ratios are expected to increase as the effective diameter increases, with little sensitivity to effective diameters larger than 100 µm. Thus, the increase of the observed τ_{vis}/τ_a with decreasing T_c could conceivably be caused by larger crystals, but this is in contradiction with the fact that mean crystal sizes and effective diameters are known to be generally decreasing with decreasing temperature for clouds of moderate optical depth smaller than 2.5 as considered in this study (see for example Heymsfield et al., 2014). Observations could also be explained by ice crystals effective diameters decreasing from 10–15 µm at T_c = 240 K down to 5 µm at T_c = 200 K, but this is very unlikely according to recent summary of in situ observations (Heymsfield et al., 2014). To go further in the discussion, ice crystal effective diameters retrieved from IIR measurements in the 3 available channels are investigated. The fundamental parameters are the so-called microphysical indices $\beta_{12/10}$ and $\beta_{12/08}$, defined as the ratios of τ_a from channel 12.05 µm to the absorption optical depths retrieved at 10.6 and at 08.65 µm, respectively. These indices can be converted into an effective diameter through Look-Up Tables, as illustrated in Fig. 7a, which shows the theoretical microphysical indices $\beta_{12/10}$ (solid lines) and $\beta_{12/08}$ (dashed lines) derived for hexagonal solid columns (blue) and aggregates (red) for τ_a = 0.25. The effective diameter is derived from the crystal model for which the relationship between $\beta_{12/10}$ and $\beta_{12/08}$ agrees the best with the observations. More details about the IIR microphysical algorithm can be found in Garnier et al. (2013). Figure 7b shows the cumulative Probability Density Function (PDF) of the derived effective diameter D_e. As discussed earlier, the analysis is applied to clouds exhibiting an optical depth $2\tau_a$ larger than 0.3, which allows minimizing possible biases in IIR retrievals at small optical depth. Still, as the IIR microphysical retrievals are the most robust for type 1 clouds with R_{BG} derived from observations as described in Garnier et al. (2013), the results are shown for type 1 clouds (green) only and by combining type 1 and type 2 clouds (black) in order to assess the impact of possible biases in the latter case. For both configurations, only 0.3 % of the retrieved diameters

AMTD
8, 2143–2189, 2015

are smaller than 15 µm, which confirms that the observed behavior of the τ_{vis}/τ_a ratios with respect to T_c cannot be explained by very small crystal sizes, especially because IIR retrievals are the most sensitive to small sizes, as evidenced in Fig. 7a.

IIR microphysical retrievals are representative of the small mode of the particle size distribution (Mitchell et al., 2010). Nonetheless, they indicate that IIR absorption optical depth is sensitive to the presence of ice crystals exhibiting these ranges in effective diameter, and the expected τ_{vis}/τ_a ratio can be estimated from the simulations shown in Fig. 2. The median expected ratios are plotted in Fig. 8a against the centroid temperature T_c (thick lines), together with the median observed ratios (thin lines) to facilitate the discussion. The green curves are for type 1 clouds whereas the black curves show the results obtained by combining type 1 and type 2 clouds. As the black and green curves are very close in the overlapping region, the analysis is conducted by combining all clouds to take advantage of the larger number of samples, especially at the coldest temperatures (Fig. 8b). The expected τ_{vis}/τ_a ratio (thick lines) steadily increases from 1.8 ± 0.1 at $T_c = 195$ K up to 1.95 ± 0.1 at T_c larger than 230 K. This result is driven by the fact that effective diameters are found increasing as temperature increases from 195 up to 230 K, and with a decreasing occurrence of hexagonal solid columns, as will be shown in Sect. 4.5.

There is an obvious disagreement between observed and expected variations with temperature of the τ_{vis}/τ_a ratios, which needs to be explained. The accuracy of the theoretical simulations is difficult to assess, but it is unlikely that they do not correctly reproduce the general behavior with respect to effective diameter. The expected τ_{vis}/τ_a ratios are weakly sensitive to the microphysical properties, so that the overall disagreement between observed and expected ratios is unlikely to be attributable to errors in IIR microphysical retrievals. On the other hand, even though CALIOP retrievals are robust because they are directly derived from the measured cloud layer two-way transmittance, the retrieved quantity is an apparent optical depth, $\tau_{apparent}$, which can be converted to the single-scattering optical depth only after applying a correction for the effect of multiple scattering on the signal measured below the cloud, which in the ver-

AMTD
8, 2143–2189, 2015

sion 3 algorithm is taken constant and equal to $\eta = 0.6$ so that

$$\tau_{\text{apparent}} = \eta \cdot \tau_{\text{vis}} = \eta_{\text{T}} \cdot \tau_{\text{vis, T}} \quad (9)$$

where η_{T} is the "true" multiple scattering correction factor, and $\tau_{\text{vis, T}}$ is the "true" single-scattering visible optical depth. It comes from Eq. (9) that variations of $\tau_{\text{vis}}/\tau_{\text{a}}$ could be driven by τ_{vis} and a correction factor η_{T}, which increases as T_{c} decreases. This tentative explanation is investigated in the following section. It is noted that a similar discussion can be found in Lamquin et al. (2008), which is based on infrared retrievals from Atmospheric Infrared Sounder (AIRS) and CALIOP co-located apparent optical depths retrieved by the authors, and where η_{T} is found larger at temperatures colder than 210 K than for cloud temperatures between 230 and 240 K.

4.4 CALIOP multiple scattering factor

In case of cirrus clouds, composed of crystals that are very large compared to CALIOP visible wavelength ($\lambda = 532$ nm), a significant fraction of the scattering energy is included in a small angle forward lobe and may stay in the lidar receiver field of view for an extended distance below the cloud base, and hence contribute to an apparent increase of the measured 2-way transmittance of the cloud. This fraction of energy varies with ice crystal phase function, ice crystal size, and lidar configuration (Nicolas et al., 1997; Chepfer et al., 1999; Hogan, 2008). The multiple scattering factor introduced by Platt (Platt, 1973; Platt et al., 2002) is a convenient parameter to correct the apparent 2-way transmittance for contribution from multiple scattering (Nicolas et al., 1997; Eloranta, 1998). This correction factor is smaller than 1, which is the single-scattering limit.

Following the approach introduced by Platt (1973), the "bulk" multiple scattering factors η_{T} derived by reconciling the observed and the expected ratios of visible optical depth to infrared absorption optical depth are now examined. For every cloud sample

AMTD
8, 2143–2189, 2015

used to build Fig. 8a, we invoke the relationship given in Eq. (9) to derive

$$\eta_T = \eta \cdot \frac{(\tau_{vis}/\tau_a)_{observed}}{(\tau_{vis}/\tau_a)_{expected}} \quad (10)$$

The 2-D-histogram of η_T (y axis) and T_c (x axis) is shown in Fig. 9a for the same data set as in Fig. 8, and by combining type 1 and type 2 clouds. The mean multiple scattering factor is found to be decreasing from $\eta_T = 0.8$ at $T_c = 200$ K to $\eta_T = 0.6$ at 220 K, and then more slowly to $\eta_T = 0.5$ at 240 K, which is the lower limit if scattering is only due to diffraction (Hogan, 2008). The overall mean value of η_T is 0.601, which is encouraging, since this is essentially identical to the constant value $\eta = 0.6$ used in the version 3 CALIOP operational algorithm. The results shown in Fig. 9 are for the 12 months of 2008. The same analysis has been applied during 2010 and 2012, and very similar results within a few percents over the whole range of temperature are obtained (not shown), with overall mean values of η_T equal to 0.604 and 0.602, respectively.

Variations of the multiple scattering factor reflect changes in the probability that a scattered photon will stay within the field of view and subsequently contribute to the measured signal. This probability becomes smaller as the lateral displacement of the photon in the clear region below the cloud increases and possibly exceeds the receiver footprint. The lateral displacement increases with the diffraction angle θ, which is inversely proportional to the ice crystal equivalent diameter D_{eq}, defined as the diameter of a sphere of equivalent volume (Nicolas et al., 1997; Comstock and Sassen, 2001). For further evaluation, the 2-D-histogram of η_T and equivalent D_{eq} derived from the IIR microphysical algorithm is shown in Fig. 9b. It is seen that, as expected, the mean value of η_T progressively departs from the single-scattering limit ($\eta_T = 1$) and decreases as D_{eq} increases or as the diffraction angle θ decreases. As the IIR effective diameter is sensitive to the small mode of the size distribution, it is a priori underestimated for many of these clouds, so that only qualitative conclusions can be drawn. Finally, the relation between η_T and a simplified estimate of the lateral displacement resulting from forward diffraction only is examined. By taking the centroid altitude Z_c as the "bulk" cloud alti-

AMTD
8, 2143–2189, 2015

tude, the distance between the diffracting ice crystals and the top of the region where the 2-way transmittance is measured is the difference between Z_c and the altitude Z_b taken 2 km below the cloud base altitude in the CALIOP algorithm, to ensure that the measurement is through the entire cloud. Thus, the lateral geometric displacement ld is roughly estimated as

$$\mathrm{ld} = \theta \cdot (Z_c - Z_b) = \frac{1.22\lambda}{D_{eq}} \cdot (Z_c - Z_b) \quad (11)$$

Figure 10a shows the mean value of the multiple scattering factor η_T as a function of the "true" visible optical depth $\tau_{vis,\,T}$ derived from Eq. (9) and of the estimated lateral displacement ld. The corresponding number of samples is shown in Fig. 10b. For most samples, optical depth is smaller than 1 and the estimated displacement ld is found to be smaller than 60 m. For comparison, the radius of the CALIOP receiver footprint is about 50 m and the radius of the laser footprint is about 42 m (Hunt et al., 2009). The mean value of η_T is found to be nicely increasing toward the single-scattering limit as the estimated value of ld increases (Fig. 10a), less rapidly as optical depth increases. It is recognized that ld is a crude estimate based on simplified geometric considerations and scattering due to diffraction only, and a quantified discussion would be hazardous. Nonetheless, these qualitative results indicate that the "bulk" multiple scattering factors η_T derived by reconciling observed and expected τ_{vis}/τ_a ratios at cloud layer scale are a real measurement of the result of the complex journey of the photons within and below the layer.

4.5 Discussion: implications for CALIOP retrievals

In this paper, CALIOP optical depths are derived from measurements of the apparent 2-way transmittance $T^2_{apparent}$. As seen in Eq. (9), the single-scattering optical depth is inversely proportional to the multiple scattering factor. According to the equation

AMTD
8, 2143–2189, 2015

introduced by Platt (1973), the apparent lidar ratio S^* can be derived as

$$S^* = \frac{1 - T^2_{\text{apparent}}}{2\gamma'} = \frac{1 - e^{-2\cdot\eta_T\cdot\tau_{\text{vis, T}}}}{2\gamma'}, \quad (12)$$

where $\gamma\prime$ is the cloud attenuated backscatter vertically integrated between layer bottom and top altitudes. The apparent lidar ratio S^* is the product of the multiple scattering factor and of the lidar ratio and is written as

$$S^* = \eta \cdot S_{\text{cal}} = \eta_T \cdot S_{\text{cal, T}}, \quad (13)$$

where S_{cal} and $S_{\text{cal, T}}$ are the lidar ratios retrieved by taking $\eta = 0.6$ and η_T from this study, respectively.

The equation introduced by Platt (1973) was established within the cloud, assuming that the multiple scattering correction factor is constant with range, which is only approximately true. In Eq. (12), a constant "bulk" correction factor η_T is considered, which is assumed to be equal to the bulk factor within the cloud. This may not be fully correct according to simulations by Winker (2003), which showed that η_T within and below the cloud could differ by about 15 %. The resulting relative error in S^* due to this approximation can be derived from Eqs. (12) and (9) as

$$\frac{dS^*}{S^*} = \frac{2\cdot\tau_{\text{apparent}}\cdot e^{-2\cdot\tau_{\text{apparent}}}}{1 - e^{-2\cdot\tau_{\text{apparent}}}} \cdot \frac{d\eta_T}{\eta_T} \quad (14)$$

As illustrated in Winker (2003), it is identical to $d\eta_T/\eta_T$ when optical depth tends to zero and decreases as optical depth increases. Subsequently, the relative error in $S_{\text{cal, T}}$ derived from Eqs. (13) and (14) is

$$\frac{dS_{\text{cal, T}}}{S_{\text{cal, T}}} = \frac{dS^*}{S^*} - \frac{d\eta_T}{\eta_T} = \left(\frac{2\cdot\tau_{\text{apparent}}\cdot e^{-2\cdot\tau_{\text{apparent}}}}{1 - e^{-2\cdot\tau_{\text{apparent}}}} - 1\right) \cdot \frac{d\eta_T}{\eta_T} \quad (15)$$

AMTD
8, 2143–2189, 2015

Here, the relative error in $S_{\mathrm{cal,\,T}}$ is null when optical depth tends to zero, and approaches progressively $-\mathrm{d}\eta_{\mathrm{T}}/\eta_{\mathrm{T}}$ as optical depth increases.

As seen in Eq. (12), the apparent lidar ratio S^* is directly derived from measurements and does not require knowledge of the multiple scattering factor. When T^2_{apparent} cannot be measured, CALIOP optical depth is derived by using the unconstrained technique, and T^2_{apparent} is retrieved from a default apparent lidar ratio, which can be established from statistical analyses of S^* retrieved from constrained retrievals (Garnier et al., 2012b). This ensures consistency between constrained and unconstrained retrievals, and in both cases, the conversion of apparent optical depth into single-scattering optical depth depends on an a priori specification of the multiple scattering factor.

Several ice crystal microphysical parameters are retrieved from the CALIPSO mission. Lidar ratios derived from measurements of the 2-way transmittance provide insights into ice crystals scattering phase function at 180°, and depolarization ratios at 532 nm are an indicator of ice crystal shape ratios (Noël et al., 2002). These measured parameters, available at global scale, have been compared with simulations for numerous ice crystal models (Baum et al., 2011). The depolarization ratio of semi-transparent cirrus clouds observed by CALIOP is not expected to be significantly impacted by the multiple scattering factor (Reichardt and Reichardt, 2003). However, the derived lidar ratio is inversely proportional to the multiple scattering factor (see Eq. 13).

The changes in optical depth and lidar ratio resulting from taking η_{T} derived in this study instead of $\eta = 0.6$ used in the standard retrieval are now examined.

4.5.1 Optical depth

The multiple scattering factor has been found to vary between $\eta_{\mathrm{T}} = 0.8$ and $\eta_{\mathrm{T}} = 0.5$ as temperature increases and to be equal to 0.6 on average. If this result is correct, then the CALIOP optical depth retrieved by using a constant value $\eta = 0.6$ is overestimated by 30 % on average at the coldest temperatures and underestimated by 15 % on average at the warmest ones. The resulting changes in optical depth histograms are shown in Fig. 11, which compares the 2-D-histograms of τ_{vis} ($\eta = 0.6$, Fig. 11a) and $\tau_{\mathrm{vis,\,T}}$ de-

AMTD
8, 2143–2189, 2015

rived from Eq. (9) (η_T, Fig. 11b) and centroid temperature, T_c. Note that in Fig. 11b, $\tau_{vis,\,T}$ is mostly larger than 0.3, because the analysis is conducted for $2\tau_a$ larger than 0.3. $\tau_{vis,\,T}$ exhibits a general increase with increasing temperature (Fig. 11b), which is not seen in τ_{vis} (Fig. 11a). This implies that on average, the extinction coefficients derived from CALIOP using η_T will increase more rapidly with temperature than those retrieved using $\eta = 0.6$. This change will also be reflected in the ice water content estimates reported in the CALIOP data products, because ice water content is inferred from a non-linear parameterization based on extinction coefficients (Heymsfield and al., 2005, 2014).

4.5.2 Microphysics

Lidar ratios with constant and variable multiple scattering factors are shown in Fig. 12, which compares the 2-D-histograms of S_{cal} ($\eta = 0.6$, Fig. 12a) and $S_{cal,\,T}$ (η_T, Fig. 12b) and centroid temperature, T_c. When η is taken constant, the median lidar ratio S_{cal} is found to be weakly varying with temperature, with a maximum $S_{cal} = 31$ sr at $T_c = 225$ K, and minima at $T_c = 200$ and 240 K that are smaller by only 10 % ($S_{cal} = 28$ sr). Because η is taken constant, we can conclude that the apparent lidar ratio S^* is likewise only weakly varying with temperature. When the multiple scattering factor is taken from this study (η_T), the temperature dependence is increased, as the median lidar ratio $S_{cal,\,T}$ is found to increase by about 50 % from $S_{cal,\,T} = 21$ sr at $T_c = 200$ K up to $S_{cal,\,T} = 34$ sr at $T_c = 228$ K, and to be roughly constant for T_c warmer than 228 K.

Distributions of the integrated volume (blue) and particulate (red) depolarization ratios reported in the CALIOP products are shown in Fig. 13a. The particulate depolarization ratio is derived from the standard extinction solutions, and thus according to this analysis should be expected to change slightly. Nevertheless, the temperature-dependent behavior of the particulate depolarization ratio is similar to the volume depolarization ratio, which indicates that contributions from molecular scattering is weak, and therefore that the current particulate depolarization ratio provides sufficient accuracy for this discussion. As for the lidar ratio $S_{cal,\,T}$, the depolarization ratio is found to

AMTD
8, 2143–2189, 2015

be essentially constant at T_c larger than 228 K, and it is found to be increasing as T_c gets colder. Furthermore, as seen in Fig. 13b, IIR retrievals indicate a decrease in the occurrence of hexagonal solid columns as T_c increases up to the same limit T_c = 228 K, with no temperature dependence at warmer temperatures. Keeping in mind that this analysis is conducted for randomly oriented ice crystals, both Fig. 13a and b suggest a progressive transition from solid columns-like crystals having large aspect shape ratios and depolarization ratios (Noël et al., 2002) at colder temperatures to more compact and less depolarizing crystals as temperatures increase. The inferred changes of crystal habit with temperature are in good agreement with in situ observations (Bailey and Hallett, 2009). Relationships between lidar ratios and depolarization ratios have been reported by numerous authors (e.g. Chen et al., 2002; Reichardt et al., 2002; Yorks et al., 2011), and correlations are expected. Overall, these observations show an apparent consistency between several independently retrieved microphysical parameters in terms of variations with layer centroid temperature. The improved correlation between depolarization ratio and lidar ratio when the latter is derived using η_T rather than by assuming a constant value is noticeable and deemed another indication of the overall consistency of our analyses.

5 Conclusions

Infrared absorption optical depths (τ_a) retrieved from IIR observations of cirrus clouds at 12.05 µm are compared to visible extinction optical depths (τ_{vis}) derived from CALIOP observations of the same cloud when direct measurements of the apparent two-way transmittance are available. IIR absorption optical depths are derived for suitable scenes selected by taking advantage of the vertical information available from collocated CALIOP observations. In this paper, we focus on single-layered cirrus clouds over ocean composed of randomly oriented ice according to CALIOP ice/water classification (high confidence) and with base temperatures colder than −20 °C.

AMTD
8, 2143–2189, 2015

IIR absorption optical depth retrievals assume an isothermal cloud with a radiative temperature inferred from the centroid altitude of the CALIOP attenuated backscatter profile. It is shown that the cloud radiative temperature can be derived a posteriori from CALIOP cloud extinction profiles, leading to quantified estimates of biases in the IIR standard products. IIR standard absorption optical depths are found to be underestimated by 1 to 17 % with biases that increase with geometric thickness and optical depth and that can be corrected a posteriori. This analysis is restricted to semi-transparent clouds with visible optical depths smaller than 2.5. In addition, IIR absorption optical depths are retrieved after correcting the observed calibrated radiances for contributions from the background radiance, which is constrained by neighboring observations if possible or otherwise derived from computations using a radiative transfer model and ancillary data. These two distinct sets of retrievals are assessed separately through comparisons with CALIOP. A better agreement of their τ_{vis}/τ_a ratios is found after correction for the cloud radiative temperature. Differences are up to 7 % at $2\tau_a = 0.7$ for the coldest clouds (203–213 K), which could be explained by biases of up to 1.1 K in the computations, even though actual differences cannot be ruled out. A specific assessment of background radiances computed in clear sky conditions is being conducted to aid in the development of future versions of the IIR data products.

Selection biases in CALIOP constrained retrievals are evidenced for visible optical depths smaller than about 0.6. The standard version 3 CALIOP constrained retrievals are conducted only when the relative uncertainty in the derived lidar ratio is estimated to be less than 40 %. When using only those optical depths originally accepted by the constrained retrieval algorithm, optical depth selection biases are seen to increase as optical depth decreases. For optical depths of 0.3, these biases introduce an overestimate of $\sim$ 50 %. Eliminating the 40 % relative uncertainty restriction substantially improves the comparisons with the IIR retrievals at small optical depths while at the same time substantially increasing the number of layers included in the study.

The retrieved τ_{vis}/τ_a ratios exhibit an unexpected quasi-linear dependence with temperature at layer centroid altitude T_c. The observed values increase by about 10 % for

AMTD
8, 2143–2189, 2015

each 10 K decrease in temperature over a range from $T_c = 240$ K down to $T_c = 200$ K. This behavior is not consistent with theoretical expectations inferred from simulations and IIR microphysical retrievals of ice crystal effective diameter D_e and most probable crystal shape. The suggested explanation is a temperature-dependent multiple scattering factor η_T, which is assumed constant and equal to 0.6 in CALIOP optical depth retrievals. This "bulk" multiple scattering factor derived by reconciling the observed and expected ratios of CALIOP visible to IIR infrared absorption optical depth is found to decrease from $\eta_T = 0.8$ at $T_c = 200$ K to $\eta_T = 0.5$ at $T_c = 240$ K for clouds of optical depth larger 0.3, and to be equal to 0.6 on average. The temperature-dependence of η_T retrieved from this study is deemed plausible according to simplified estimates of key parameters driving the multiple scattering factor. The next steps in the assessment would be to perform detailed simulations in order to improve the accuracy of the current results.

These findings imply that CALIOP optical depth and extinction coefficients are on average overestimated by about 30 % at $T_c = 200$ K and underestimated by about 15 % at $T_c = 240$ K for the data set selected in this study. This statement would need to be confirmed through comparisons with retrievals from other instruments. The apparent consistency between several independently retrieved microphysical parameters, namely the integrated depolarization ratio, the ice crystal shape occurrence derived from the IIR, and the lidar ratio is reinforced when the latter is derived from η_T rather than by assuming a constant value. The increased correlation between lidar ratio and depolarization ratio is considered to be further evidence that the η_T parameterization more accurately reflects the underlying microphysics of cirrus clouds. These results could contribute to a better characterization of optically thin cirrus clouds at night over ocean, with subsequent opportunities for improved understanding of possible formation mechanisms.

This paper illustrates the added value of synergetic analyses of perfectly collocated retrievals from the IIR passive radiometer and from the CALIOP active lidar. Understanding and estimating biases, even for a limited data set, allows refining uncertainty

AMTD
8, 2143–2189, 2015

estimates and improving the full consistency of the retrievals, and provides guidance for the development of future versions of the products. Continuous assessment and improvement of the CALIPSO data record, both in the visible and in thermal infrared spectral domains, is of importance for a better understanding of the radiative impact of cirrus clouds at global scale, as CALIPSO has now reached an unprecedented duration of 8 years in orbit.

Acknowledgements. The authors thank Steve Platnick and Bob Holz for many fruitful discussions about active and passive remote sensing retrievals and thank Ping Yang for providing the ice crystal optical properties used in our simulation studies. The authors are grateful to the ICARE data center in France for their help with the development of the IIR Level 2 algorithm. CALIPSO products are publicly available at the Atmospheric Science Data Center of the NASA Langley Research Center and at ICARE data center. The authors are thankful to Patricia Lucker for her support, to CNES, and to CNRS (Centre National de la Recherche Scientifique).

References

Bailey, M. and Hallett, J.: A comprehensive habit diagram for atmospheric ice crystals: confirmation from the laboratory, AIRS II, and other field studies, J. Atmos. Sci., 66, 2888–2899, 2009.

Baum, B. A., Yang, P., Heymsfield, A. J., Schmitt, C. G., Xie, Y., Bansemer, A., Hu, Y.-X., and Zhang, Z.: Improvements in shortwave bulk scattering and absorption models for the remote sensing of ice clouds, J. Appl. Meteorol. Clim., 50, 1037–1056, doi:10.1175/2010JAMC2608.1, 2011.

Berry, E. and Mace, G. G.: Cloud properties and radiative effects of the Asian summer monsoon derived from A-Train data, J. Geophys. Res., 119, 9492–9508, doi:10.1002/2014JD021458, 2014.

Chen, W. N., Chiang, C. W., and Nee, J. B.: Lidar ratio and depolarization ratio for cirrus clouds, Appl. Optics, 41, 6470–6476, doi:10.1364/AO.41.006470, 2002.

Chepfer, H., Pelon, J., Brogniez, G., Flamant, C., Trouillet, V., and Flamant, P. H.: Impact of cirrus cloud ice crystal shape and size on multiple scattering effects: application to spaceborne

AMTD
8, 2143–2189, 2015

and airborne backscatter lidar measurements during LITE mission and E-LITE campaign, Geophys. Res. Lett., 26, 2203– 2206, 1999.
Comstock, J. and Sassen, K.: Retrieval of cirrus cloud radiative and backscattering properties using combined lidar and infrared radiometer (LIRAD) measurements, J. Atmos. Ocean. Tech., 18, 1658–1673, 2001.
Corlay, G., Arnolfo, M.-C., Bret-Dibat, T., Lifermann, A., and Pelon, J.: The infrared imaging radiometer for PICASSO-CENA, available at: http://smsc.cnes.fr/CALIPSO/IIR_ICSO00_S2-06.pdf (last access: 23 February 2015), 2000.
Del Guasta, M.: Errors in the retrieval of thin-cloud optical parameters obtained with a two-boundary algorithm, Appl. Optics, 37, 5522–5540, 1998.
Dubuisson, P., Giraud, V., Chomette, O., Chepfer, H., and Pelon, J.: Fast radiative transfer modeling for infrared imaging radiometry, J. Quant. Spectrosc. Ra., 95, 201–220, 2005.
Dubuisson, P., Giraud, V., Pelon, J., Cadet, B., and Yang, P.: Sensitivity of thermal infrared radiation at the top of the atmosphere and the surface to ice cloud microphysics. J. Appl. Meteorol. Clim., 47, 2545–2560, 2008.
Eloranta, E. W.: A practical model for the calculation of multiply scattered lidar returns, Appl. Optics, 37, 2464–2472, 1998.
Elouragini, S. and Flamant, P. H.: Iterative method to determine an averaged backscatter-to-extinction ratio in cirrus clouds, Appl. Optics, 35, 1512–1518, 1996.
Garnier, A., Pelon, J., Dubuisson, P., Faivre, M., Chomette, O., Pascal, N., and Kratz, D. P.: Retrieval of cloud properties using CALIPSO Imaging Infrared Radiometer. Part I: effective emissivity and optical depth, J. Appl. Meteorol. Clim., 51, 1407–1425, doi:10.1175/JAMC-D-11-0220.1, 2012a.
Garnier, A., Vaughan, M. A., Dubuisson, P., Josset, D., Pelon, J., and Winker, D. M.: Multi-sensor cirrus optical depth estimates from CALIOP, in: Reviewed & Revised Papers Presented at the 26th International Laser Radar Conference, Porto Heli, Greece, 25–29 June 2012, 691–694, 2012b.
Garnier, A., Pelon, J., Dubuisson, P., Yang, P., Faivre, M., Chomette, O., Pascal, N., Lucker, P., and Murray, T.: Retrieval of cloud properties using CALIPSO Imaging Infrared Radiometer. Part II: effective diameter and ice water path, J. Appl. Meteorol. Clim., 52, 2582–2599, doi:10.1175/JAMC-D-12-0328.1, 2013.

AMTD
8, 2143–2189, 2015

Heymsfield, A., Winker, D., and van Zadelhoff, G.-J.: Extinction-ice water content-effective radius algorithms for CALIPSO, Geophys. Res. Lett., 32, L10807, doi:10.1029/2005GL022742, 2005.

Heymsfield, A., Winker, D., Avery, M., Vaughan, M., Diskin, G., Deng, M., Mitev, V., and Matthey, R.: Relationships between ice water content and volume extinction coefficient from in situ observations for temperatures from 0 to −86 °C: implications for spaceborne lidar retrievals, J. Appl. Meteorol. Clim., 53, 479–505, doi:10.1175/JAMC-D-13-087.1, 2014.

Hogan, R. J.: Fast lidar and radar multi-scattering models. Part I: Small-angle scattering using the photon variance-covariance method, J. Atmos. Sci., 65, 3621–3635, 2008.

Hu, Y., Vaughan, M., Liu, Z., Powell, K., and Rodier, S.: Retrieving optical depths and lidar ratios for transparent layers above opaque water clouds from CALIPSO lidar measurements, IEEE Geosci. Remote S., 4, 523–526, doi:10.1109/LGRS.2007.901085, 2007.

Hu, Y., Winker, D., Vaughan, M., Lin, B., Omar, A., Trepte, C., Flittner, D., Yang, P., Nasiri, S. L., Baum, B., Holz, R., Sun, W., Liu, Z., Wang, Z., Young, S., Stamnes, K., Huang, J., and Kuehn, R.: CALIPSO/CALIOP cloud phase discrimination algorithm, J. Atmos. Ocean. Tech., 26, 2293–2309, doi:10.1175/2009JTECHA1280.1, 2009.

Hu, Y., Rodier, S., Xu, K., Sun, W., Huang, J., Lin, B., Zhai, P., and Josset, D.: Occurrence, liquid water content, and fraction of supercooled water clouds from combined CALIOP/IIR/MODIS measurements, J. Geophys. Res., 115, D00H34, doi:10.1029/2009JD012384, 2010.

Hunt, W. H., Winker, D. M., Vaughan, M. A., Powell, K. A., Lucker, P. L., and Weimer, C.: CALIPSO lidar description and performance assessment, J. Atmos. Ocean. Tech., 26, 1214–1228, doi:10.1175/2009JTECHA1223.1, 2009.

Josset, D., Pelon, J., Garnier, A., Hu, Y- X., Vaughan, M., Zhai, P., Kuehn, R., and Lucker, P.: Cirrus optical depth and lidar ratio retrieval from combined CALIPSO-CloudSat observations using ocean surface echo, J. Geophys. Res., 117, D05207, doi:10.1029/2011JD016959, 2012.

Lamquin, N., Stubenrauch, C. J., and Pelon, J.: Upper tropospheric humidity and cirrus geometrical and optical thickness: relationships inferred from one year of collocated AIRS and CALIPSO data, J. Geophys. Res., 113, D00A08, doi:10.1029/2008JD010012, 2008.

Liu, Z., Vaughan, M. A., Winker, D. M., Kittaka, C., Getzewich, B. J., Kuehn, R. E., Omar, A., Powell, K. A., Trepte, C. R., and Hostetler, C. A.: The CALIPSO lidar cloud and aerosol discrimination: version 2 algorithm and initial assessment of performance, J. Atmos. Ocean. Tech., 26, 1198–1213, 2009.

AMTD
8, 2143–2189, 2015

Mitchell, D. L.: Effective diameter in radiation transfer: general definition, applications, and limitations, J. Atmos. Sci., 59, 2330–2346, 2002.
Mitchell, D. L., d'Entremont, R. P., and Lawson, R. P.: Inferring cirrus size distributions through satellite remote sensing and microphysical databases, J. Atmos. Sci., 67, 1106–1125, doi:10.1175/2009JAS3150.1, 2010.
Nicolas, F., Bissonnette, L. R., and Flamant, P. H.: Lidar effective multiple-scattering coefficients in cirrus clouds, Appl. Optics, 36, 3458–3468, 1997.
Noël, V., Chepfer, H., Ledanois, G., Delaval, A., and Flamant, P. H.: Classification of particle shape ratios in cirrus clouds based on the lidar depolarization ratio, Appl. Optics, 41, 4245–4257, 2002.
Pitts, M. C., Thomason, L. W., Hu, Y., and Winker, D. M.: An assessment of the on-orbit performance of the CALIPSO Wide Field Camera, in: Remote Sensing of Clouds and the Atmosphere XII, SPIE Proceedings, vol. 6745, edited by: Comeron, A., Schäfer, K., Slusser, J. R., Picard, R. H., and Amodeo, A., International Society for Optical Engineering, Florence, Italy, 67450K, doi:10.1117/12.737377, 2007.
Platt, C. M. R.: Lidar and radiometric observations of cirrus clouds, J. Atmos. Sci., 30, 1191–1204, 1973.
Platt, C. M. R. and Gambling, D. J.: Emissivity of high layer clouds by combined lidar and radiometric techniques, Q. J. Roy. Meteor. Soc., 97, 322–325, 1971.
Platt, C. M. R., Young, S. A., Austin, R. T., Patterson, G. R., Mitchell, D. L., and Miller, S. D.: LIRAD observations of tropical cirrus clouds in MCTEX. Part I: Optical properties and detection of small particles in cold cirrus, J. Atmos. Sci., 59, 3145–3162, 2002.
Powell, K., Vaughan, M., Winker, D., Lee, K.-P., Pitts, M., Trepte, C., Detweiler, P., Hunt, W., Lambeth, J., Lucker, P., Murray, T., Hagolle, O., Lifermann, A., Faivre, M., Garnier, A., and Pelon, J.: CALIPSO data management systems data products catalog, document No. PC-SCI-503, Release 3.6, available at: http://www-calipso.larc.nasa.gov/products/CALIPSO_DPC_Rev3x6.pdf (last access: 23 February 2015), 2013.
Reichardt, J., Reichardt, S., Hess, M., and McGee, T. J.: Correlations among the optical properties of cirrus-cloud particles: microphysical interpretation, J. Geophys. Res., 107, 4562, doi:10.1029/2002JD002589, 2002.
Reichardt, S. and Reichardt, J.: Effect of multiple scattering on depolarization measurements with spaceborne lidars, Appl. Optics, 42, 3620–3633, 2003.

AMTD
8, 2143–2189, 2015

Rienecker, M. M., Suarez, M. J., Todling, R., Bacmeister, J., Takacs, L., Liu, H.-C., Gu, W., Sienkiewicz, M., Koster, R. D., Gelaro, R., Stajner, I., and Nielsen, J. E.: The GEOS-5 Data Assimilation System – Documentation of Versions 5.0.1, 5.1.0, and 5.2.0, Technical Report Series on Global Modeling and Data Assimilation, 27, NASA/TM-2008-104606, 1–118, 2008.

Sassen, K., Wang, Z., and Liu, D.: Global distribution of cirrus clouds from CloudSat/Cloud-Aerosol Lidar and Infrared Pathfinder Satellite Observations (CALIPSO) measurements, J. Geophys. Res., 113, D00A12, doi:10.1029/2008JD009972,2008.

Sourdeval, O., Brogniez, G., Pelon, J., Labonnote, L. C., Dubuisson, P., Parol, F., Josset, D., Garnier, A., Faivre, M., and Minikin, A.: Validation of IIR/CALIPSO level 1 measurements by comparison with collocated airborne observations during CIRCLE-2 and Biscay '08 Campaigns, J. Atmos. Ocean. Tech., 29, 653–667, doi:10.1175/JTECH-D-11-00143.1, 2012.

Vaughan, M. A., Winker, D. M., and Powell, K. A.: CALIOP Algorithm Theoretical Basis Document. Part 2: Feature Detection and Layer Properties Algorithms, PC-SCI-202.02, NASA Langley Research Center, Hampton, VA 23681, 87 pp., available at: http://www-calipso.larc.nasa.gov/resources/project_documentation.php (last access: 23 February 2015), 2005.

Vaughan, M. A., Powell, K. A., Winker, D. M., Hostetler, C. A., Kuehn, R. E., Hunt, W. H., Getzewich, B. J., Young, S. A., Liu, Z., and McGill, M. J.: Fully automated detection of cloud and aerosol layers in the CALIPSO lidar measurements, J. Atmos. Ocean. Tech., 26, 2034–2050, doi:10.1175/2009JTECHA1228.1, 2009.

Winker, D. M.: Accounting for multiple scattering in retrievals from space lidar, Proc. SPIE Int. Soc. Opt. Eng., 5059, 128–139, 2003.

Winker, D. M., Vaughan, M. A., Omar, A. H., Hu, Y., Powell, K. A., Liu, Z., Hunt, W. H., and Young, S. A.: Overview of the CALIPSO mission and CALIOP data processing algorithms, J. Atmos. Ocean. Tech., 26, 2310–2323, doi:10.1175/2009JTECHA1281.1, 2009.

Winker, D. M., Pelon, J., Coakley Jr., J. A., Ackerman, S. A., Charlson, R. J., Colarco, P. R., Flamant, P., Fu, Q., Hoff, R., Kittaka, C., Kubar, T. L., LeTreut, H., McCormick, M. P., Megie, G., Poole, L., Powell, K., Trepte, C., Vaughan, M. A., and Wielicki, B. A.: The CALIPSO mission: a global 3-D view of aerosols and clouds, B. Am. Meteorol. Soc., 91, 1211–1229, 2010.

Yang, P., Wei., H., Huang, H. L., Baum, B. A., Hu, Y. X., Kattawar, G. W., Mishchenko, M. I., and Fu, Q.: Scattering and absorption property database for non-spherical ice particles in the near- through far-infrared spectral region, Appl. Optics, 44, 5512–5523, 2005.

AMTD
8, 2143–2189, 2015

Yorks, J. E., Hlavka, D. L., Hart, W. D., and McGill, M. J.: Statistics of cloud optical properties from airborne lidar measurements, J. Atmos. Ocean. Tech., 28, 869–883, doi:10.1175/2011JTECHA1507.1, 2011.

Young, S. A.: Analysis of lidar backscatter profiles in optically thin clouds, Appl. Optics, 34, 7019–7031, doi:10.1364/AO.34.007019, 1995.

Young, S. A. and Vaughan, M. A.: The retrieval of profiles of particulate extinction from Cloud-Aerosol Lidar Infrared Pathfinder Satellite Observations (CALIPSO) data: algorithm description, J. Atmos. Ocean. Tech., 26, 1105–1119, 2009.

Young, S. A., Vaughan, M. A., Kuehn, R. E., and Winker, D. M.: The retrieval of profiles of particulate extinction from Cloud-Aerosol Lidar Infrared Pathfinder Satellite Observations (CALIPSO) data: uncertainty and error sensitivity analyses, J. Atmos. Ocean. Tech., 30, 395–428, doi:10.1175/JTECH-D-12-00046.1, 2013.

AMTD
8, 2143–2189, 2015

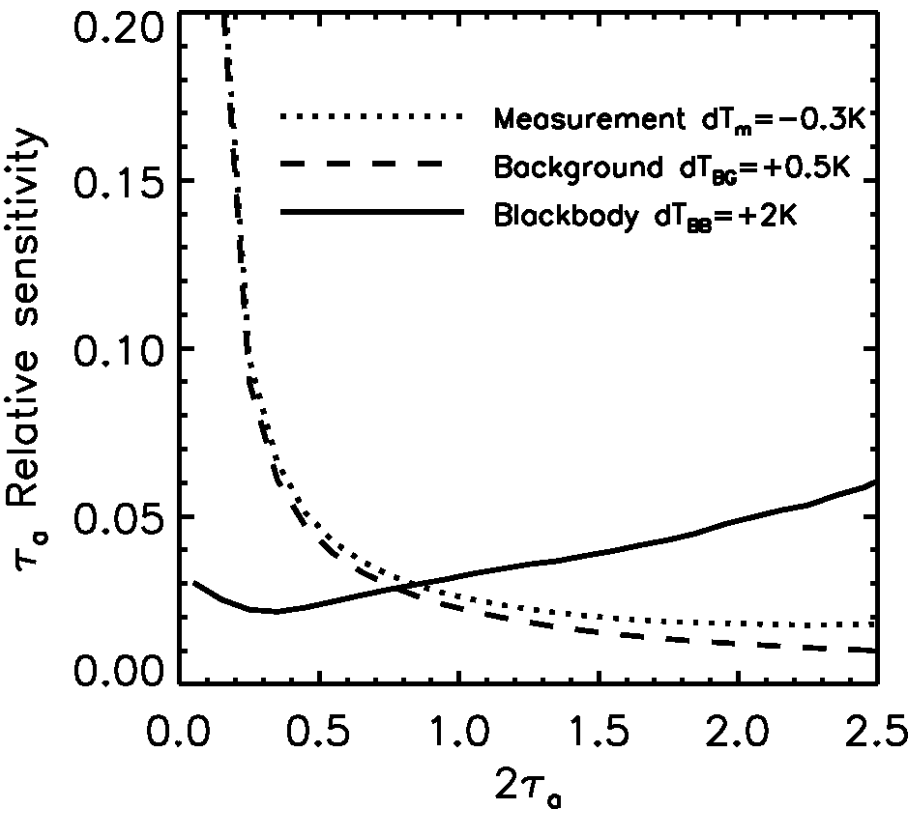

Figure 1. Relative sensitivity of absorption optical depth τ_a to variations of measured (dotted), background (dashed) and blackbody (solid) brightness temperatures $dT_m = -0.3$ K, $dT_{BG} = 0.5$ K, and $dT_{BB} = 2$ K, respectively.

AMTD
8, 2143–2189, 2015

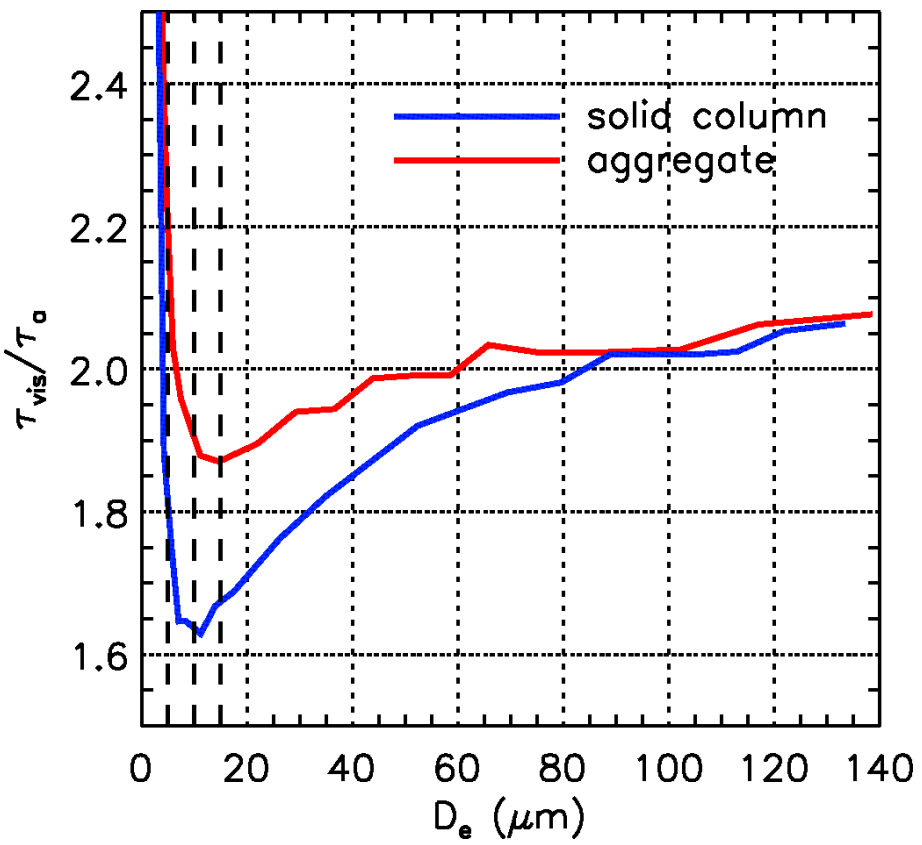

Figure 2. Simulations of the ratio between CALIOP optical depth at 532 nm (τ_{vis}) and IIR absorption optical depth at 12.05 µm (τ_a) at τ_a = 0.25 against effective diameter D_e for hexagonal solid columns (blue) and aggregates (red). Vertical dashed lines indicate D_e smaller than 15 µm (see text).

AMTD
8, 2143–2189, 2015

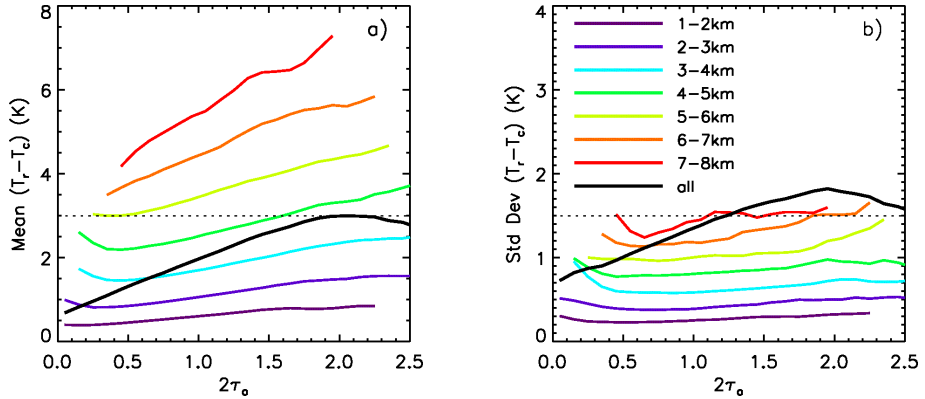

Figure 3. (a) Mean value and **(b)** standard deviation of the difference $T_r - T_c$ between cloud radiative temperature and temperature at centroid altitude of attenuated total backscatter against $2\tau_a$ assuming $r = \tau_{vis}/\tau_a = 2$. Colored lines are for several ranges in cloud geometric thickness. The black line is for all samples. The horizontal dotted lines indicate maximum values discussed in the text. Data set: single-layered cirrus ROI with high confidence, base temperature $< -20\,^{\circ}C$, over ocean, 2008.

AMTD
8, 2143–2189, 2015

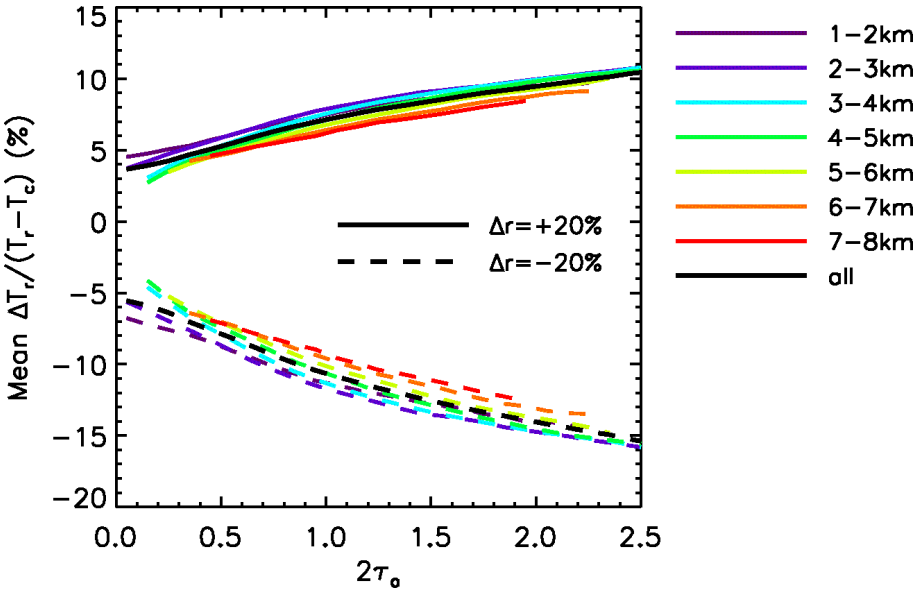

Figure 4. Relative sensitivity (in percentage) of the difference $T_r - T_c$ to a variation of $\Delta r = +20\,\%$ (solid lines) and $\Delta r = -20\,\%$ (dashed lines) of the assumed τ_{vis}/τ_a ratio $r = 2$. Colored lines are for several ranges in cloud geometric thickness Δz. The black lines are for all samples. Same data set as in Fig. 3.

AMTD
8, 2143–2189, 2015

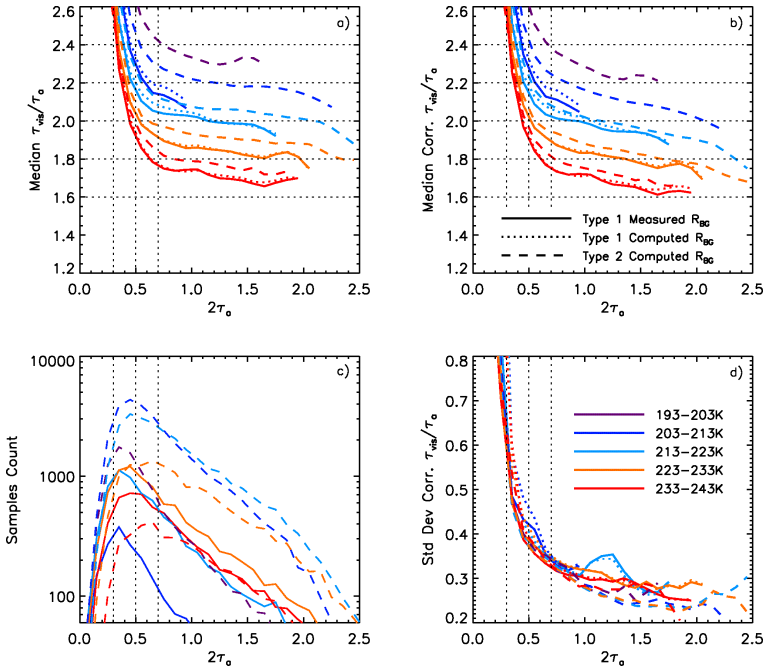

Figure 5. Median τ_{vis}/τ_a ratio against $2\tau_a$ **(a)** from IIR standard products and **(b)** after correction for cloud radiative temperature, **(c)** samples count, and **(d)** τ_{vis}/τ_a ratio standard deviation. Type 1 clouds: measured R_{BG} available and τ_a either from measured R_{BG} (solid) or from computed R_{BG} (dotted); Type 2 clouds: no measured R_{BG} available and R_{BG} from computations (dashed). Colors are for temperature at centroid altitude T_c in 193–203 K (purple), 203–213 K (navy blue), 213–223 K (light blue), 223–233 K (orange), and 233–243 K (red). The vertical dotted lines highlight the results for $2\tau_a$ between 0.3 and 0.7 (see text). Data set: single-layered cirrus ROI with high confidence, base temperature < −20 °C, over ocean, 25° S–25° N, 2008.

AMTD
8, 2143–2189, 2015

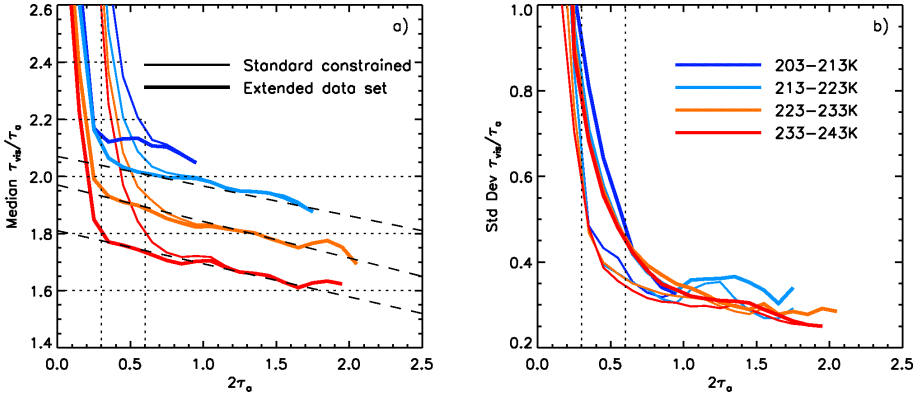

Figure 6. (a) Median τ_{vis}/τ_a ratio and **(b)** standard deviation from standard CALIOP constrained retrievals (thin lines) and from extended CALIOP optical depth measurements (thick lines) for type 1 clouds retrieved from measured R_{BG} after correction for cloud radiative temperature. The vertical dotted lines highlight the differences for $2\tau_a$ between 0.3 and 0.6 (see text). Same data set and color code as in Fig. 5.

AMTD
8, 2143–2189, 2015

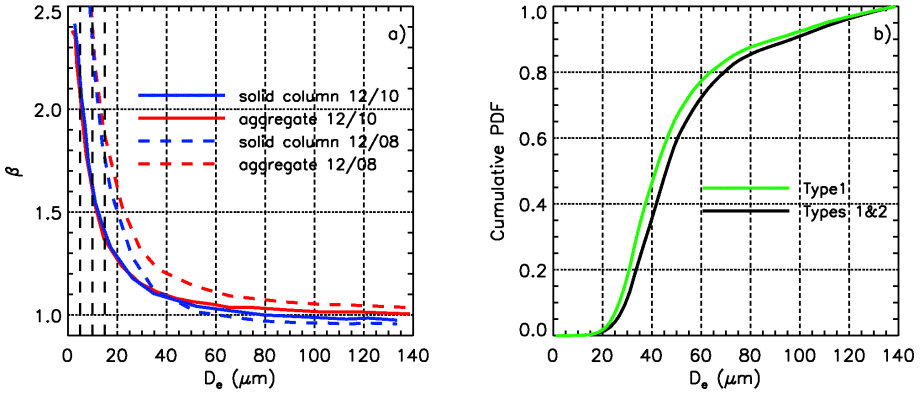

Figure 7. (a) Theoretical microphysical indices $\beta_{12/10}$ (solid lines) and $\beta_{12/08}$ (dashed lines) against effective diameter D_e for a cloud composed of hexagonal solid columns (blue) and of aggregates (red), with $\tau_a = 0.25$. The vertical dashed lines highlight the large sensitivity to D_e smaller than 15 µm (see text). **(b)** Cumulative Probability Density Function (PDF) of D_e retrieved from IIR microphysical indices for type 1 clouds (green, measured R_{BG}) and by combining type 1 and type 2 clouds (black). Data set: single-layered cirrus ROI with high confidence, base temperature < −20 °C, extended CALIOP optical depth measurements, $2\tau_a > 0.3$, over ocean, 2008.

AMTD
8, 2143–2189, 2015

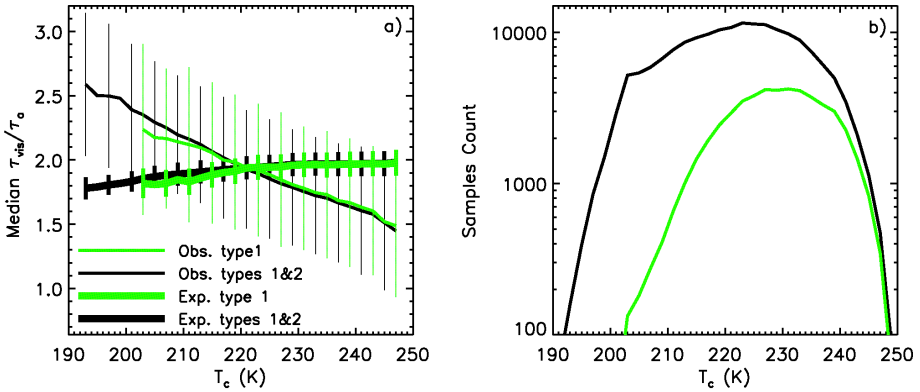

Figure 8. (a) Median observed (thin lines) and expected (thick lines) τ_{vis}/τ_a ratio ± standard deviation and **(b)** associated samples count against temperature T_c for type 1 clouds (green, measured R_{BG}) and combined type 1 and type 2 clouds (black). Same data set as in Fig. 7b.

AMTD
8, 2143–2189, 2015

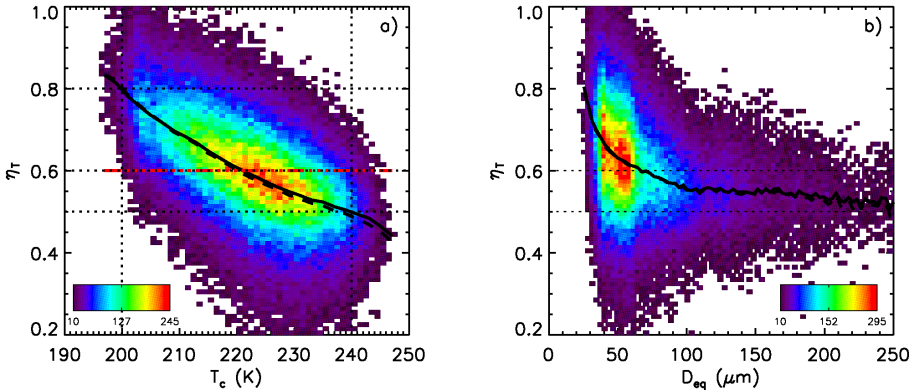

Figure 9. 2-D-histogram of multiple scattering factor η_T and **(a)** temperature T_c, and **(b)** equivalent diameter D_{eq}. The color code is the number of samples. The median and mean values against T_c are the black solid and dashed lines, respectively. In Fig. 9a, the horizontal red dotted dashed line shows the mean value of η_T overall (0.601). The dotted lines indicate values discussed in the text. Same data set as in Fig. 8, all clouds combined.

AMTD
8, 2143–2189, 2015

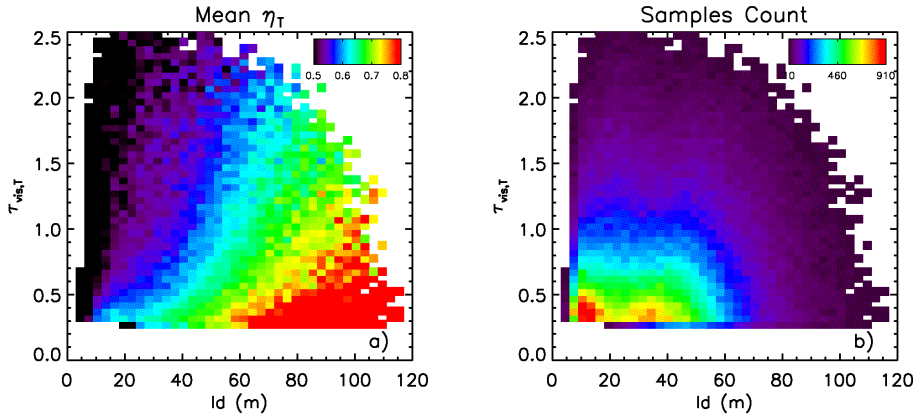

Figure 10. (a) Mean value of the multiple scattering factor η_T as a function of visible optical depth $\tau_{vis,\,T}$ and estimated lateral displacement ld; **(b)** associated number of samples. Same data set as in Fig. 9.

AMTD
8, 2143–2189, 2015

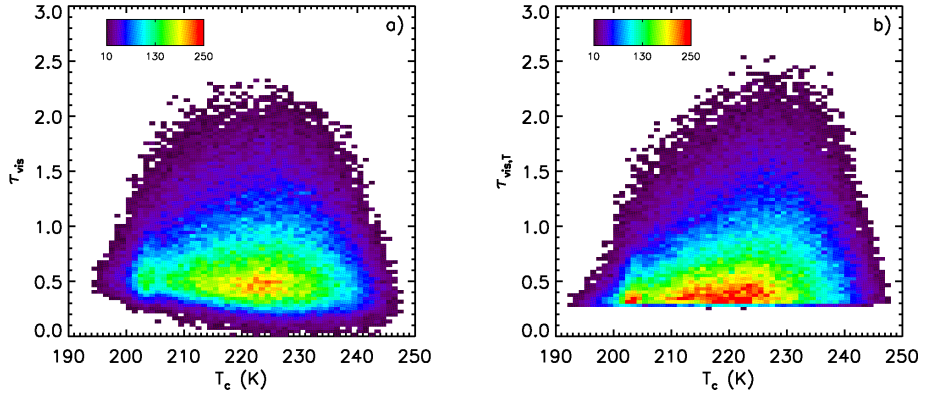

Figure 11. 2-D-histogram of **(a)** τ_{vis} ($\eta = 0.6$) and **(b)** $\tau_{vis,T}$ (η_T from this study), and centroid temperature T_c. The color code is the number of samples. Same data set as in Fig. 9.

AMTD
8, 2143–2189, 2015

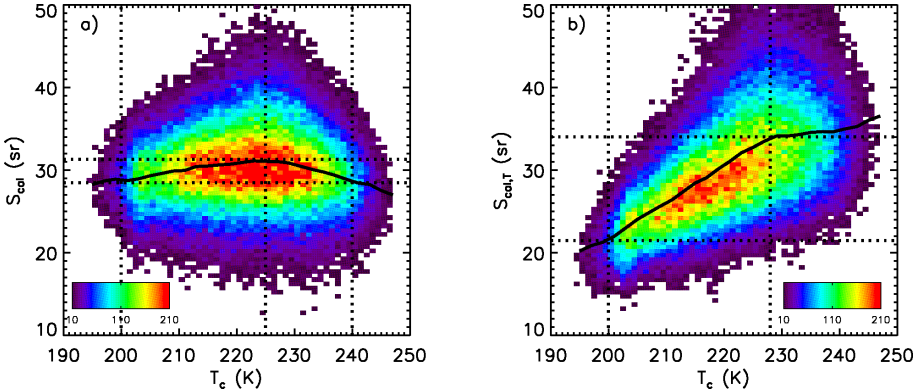

Figure 12. 2-D-histogram of lidar ratio **(a)** S_{cal} ($\eta = 0.6$) and **(b)** $S_{cal,\,T}$ (η_T from this study), and centroid temperature T_c. The color code is the number of samples. The black solid line is the median value. The dotted lines indicate minimum and maximum values and associated temperatures (see text). Same data set as in Fig. 9.

AMTD
8, 2143–2189, 2015

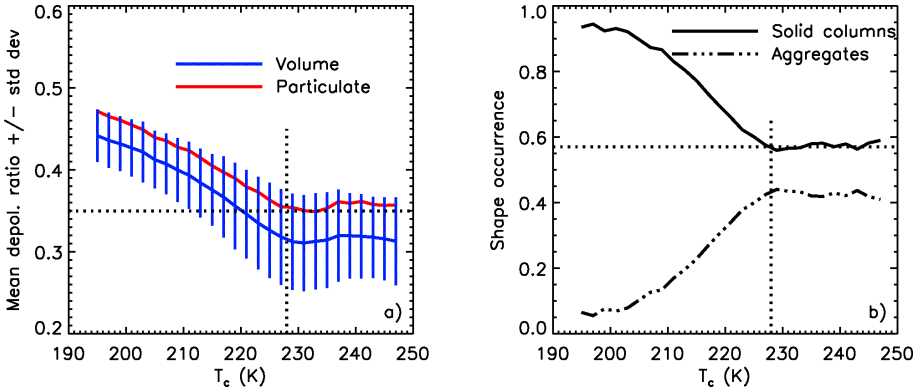

Figure 13. (a) Mean ± SD volume (blue) and particulate (red) depolarization ratio against T_c; **(b)** IIR retrieved shape occurrence against T_c. The dotted lines indicate variations with T_c discussed in the text. Same data set as in Fig. 9.

AMTD
8, 2143–2189, 2015